Check for updates

An ultra-stable bio-inspired bacteriochlorin analogue for hypoxia-tolerant photodynamic therapy†

Mengsi Wu,‡ Zhiyong Liu‡ and Weian Zhang [ID] *

Photodynamic therapy (PDT) greatly suffers from the weak NIR-absorption, oxygen dependence and poor stability of photosensitizers (PSs). Herein, inspired by natural bacteriochlorin, we develop a bacteriochlorin analogue, tetrafluorophenyl bacteriochlorin (**FBC**), by one-step reduction of tetrafluorophenyl porphyrin (**TFPP**). **FBC** can realize deep tissue penetration, benefitting from the strong NIR absorption. The reactive oxygen species (ROS) generation capacity of **FBC** can retain around 60% with a 1.0 cm-thick pork skin as the barrier. Besides, **FBC** could not only produce oxygen-dependent $^1O_2$, but also generate less oxygen-dependent $O_2^{-\cdot}$ and $\cdot$OH to achieve excellent PDT even in hypoxic tumors. Moreover, **FBC** exhibits an ultra-high stability and it is almost unchanged even under visible light at room temperature for 15 months. Interestingly, the high reactivity of the fluorophenyl group makes it easy for **FBC** to produce **FBC** derivatives. A biocompatible **FBC** nanogel could be directly formed by blending **FBC** with SH–PEG–SH. The **FBC** nanogel displays excellent photodynamic efficacy *in vitro* and *in vivo*. Thus, **FBC** would be a promising PS for the clinical PDT of deep tumors.

Introduction

Photodynamic therapy (PDT) is an attractive approach for tumor inhibition due to its advantages of being non-invasive, and having weak adverse effects and spatiotemporal control.[1,2] However, the clinical utility of PDT is greatly limited by the inadequate NIR absorption, oxygen dependence and poor stability of conventional photosensitizers (PSs) such as photofin, verteporfin and padeliporfin. Short wavelength light absorbed by PSs cannot reach deep tissue due to absorption of skin and subcutaneous adipose tissue, resulting in lower photoconversion, serious tissue damage and limited clinical application of PDT in deep tumors.[3] To address this issue, some strategies such as the two-photon excitation (TPE) technique[4,5] and upconversion nanoparticles (UCNPs)[6,7] had been introduced for the therapy of deep tumors, but their complex equipment and their low conversion efficiency will bring about new problems for clinical applications.[8,9] Thus, PSs with strong NIR (700–1000 nm) absorption, which display deeper tissue penetration and minimized photodamage, have attracted intense research efforts for eradicating tumors in deep sites.[10–12] Moreover, PDT efficacy also greatly suffers from the hypoxic environment of solid tumors, since conventional PSs consume

oxygen to produce reactive oxygen species (ROS) for inhibiting tumor growth (type II mechanism). A great number of contributions have been recently dedicated to defeating the hypoxia of tumors by increasing oxygen concentration,[13,14] including *in situ* oxygen production at tumor sites *via* catalytic reactions[15–17] and oxygen delivery into tumors.[18,19] Besides the elevation of oxygen concentration, exploiting photosensitizers that produce ROS through a less oxygen-dependent mechanism (type I mechanism) is a prospective approach to overcome the limitations of hypoxia.[20,21] Additionally, some PSs are unstable towards oxygen and light. The photobleaching of PSs significantly reduces the efficacy of PDT, hindering the clinical application of PDT.[22–25] Therefore, to achieve clinical treatment of deep tumors, it is urgent to develop highly stable, less oxygen-dependent PSs with strong NIR absorption for enhancing PDT efficacy.

Besides, most traditional PSs are hydrophobic conjugated macrocycle compounds, and they often could not produce high PDT efficiency due to their fatal disadvantages including poor solubility, the aggregation-caused quenching (ACQ) effect and inappropriate selectivity.[26–28] To enhance PDT efficiency, many strategies have been explored to enrich PSs at tumor sites.[29–31] For example, a series of nano-carriers have been developed to load and deliver hydrophobic PSs.[32–34] Nevertheless, some irreparable deficiencies of nano-carriers such as low loading efficiency, non-repeatability, drug leakage and carrier-induced toxicity severely limit the development of their large-scale applications.[35,36] Recently, nanogels have received great attention for delivering and enriching drugs into tumors upon incorporating hydrophobic drugs into the gel network,[37,38] since

Shanghai Key Laboratory of Functional Materials Chemistry, East China University of Science and Technology, 130 Meilong Road, Shanghai 200237, China

† Electronic supplementary information (ESI) available. See DOI: 10.1039/d0sc05525e

‡ These authors contributed equally.

they not only possess many promising hydrogel features such as high drug-loading efficiency, water-solubility, and biocompatibility for delivery of hydrophobic drugs, but also exhibit size in the nanoscale range for accumulation of drugs at tumor sites by the enhanced permeability and retention (EPR) effect. Given that hydrophobic PSs are incorporated into nanogel networks to form PS-based nanogels, except for the above advantageous properties of nanogels, the ACQ effect of PSs could be inhibited effectively since PS units are fixed on network knots to prevent aggregation.[39]

Inspired by the strong NIR absorption of natural bacteriochlorin, we developed a bacteriochlorin-based photosensitizer tetrafluorophenyl bacteriochlorin (**FBC**) by one-step reduction of tetrafluorophenyl porphyrin (**TFPP**). **FBC** could be further utilized to prepare a hydrophilic **FBC** nanogel by directly mixing with HS-terminated telechelic poly(ethylene glycol) (HS-PEG-SH), due to the high reactivity of the *p*-F atom of fluorophenyl in **FBC**. The **FBC** nanogel as a novel nano-photosensitizer possesses the following advantages (Scheme 1): (i) strong NIR absorption of **FBC** at 750 nm endows the **FBC** nanogel with deep tissue permeability, realizing the possibility of PDT against deep tumors. (ii) **FBC** could not only produce oxygen-dependent singlet oxygen (type II), but also generate less oxygen-dependent ROS (type I), achieving excellent PDT even in hypoxic tumors. (iii) **FBC** has an ultra-high stability under visible light at room temperature, showing the potential for clinical applications. (iv) **FBC** could be facilely obtained by two-step reactions from the original reactive agents pentafluorobenzaldehyde and pyrrole, providing an opportunity as a novel commercial photosensitizer. (v) The *p*-F atom of fluorophenyl in **FBC** is highly reactive, making it easy to prepare **FBC** derivatives. (vi) The formation of the **FBC** nanogel improves the PDT efficacy due to the high drug loading efficiency, biocompatibility and reduced ACQ effect of PSs. Consequently, the **FBC**-based nanophotosensitizer would be a promising candidate for NIR-mediated PDT against hypoxic tumors at deep sites.
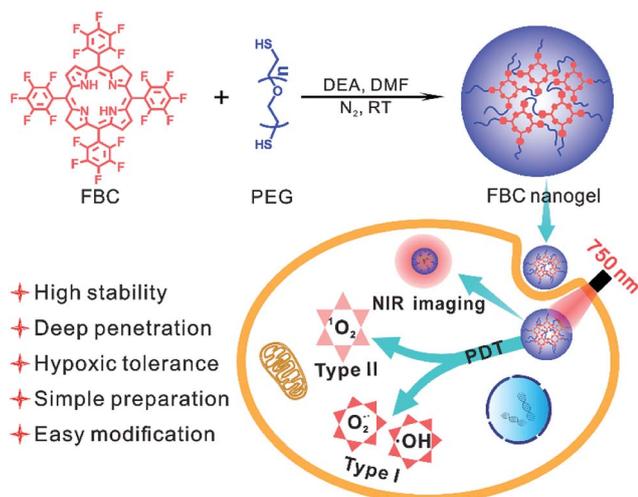
Scheme 1 Illustration of the **FBC** nanogel synthesis and the mechanism of the PDT performance of the **FBC** nanogel.

Results and discussion

Synthesis of FBC

Bacteriochlorins extracted from bacteria have presented great promising application in PDT, since they exhibit a strong absorption in the near-infrared region. But, the difficult preparation, low yield and poor stability of bacteriochlorins limited their applications.[25,40] Inspired by the structure of bacteriochlorins, an analogue of bacteriochlorin, **FBC**, was synthesized *via* one-step diimide reduction of **TFPP**. **TFPP** could be directly obtained using the original reactive agents pentafluorobenzaldehyde and pyrrole, according to previous studies.[41,42] As shown in Scheme S1 (ESI†), **TFPP** was carefully mixed with *p*-toluenesulfonyl hydrazide (TSH) by grinding, and then the mixture was heated under vacuum to produce **FBC** after 2 h of vacuuming. **FBC** was characterized with ^{1}H-NMR and ^{19}F-NMR spectra (Fig. S1–S5, ESI†). Compared to that of to **TFPP**, a new peak at 4 ppm appeared in Fig. S4 (ESI†), indicating that **TFPP** was reduced to **FBC**. Additionally, the successful synthesis of **FBC** was also confirmed by mass spectrometry (Fig. S3 and S6, ESI†).

Penetration ability of FBC

The photophysical features of **FBC** were determined by UV-vis spectroscopy and fluorescence spectroscopy, as shown in Fig. 1a and S7 (ESI†). It can be observed that a strong absorbance and emission peak separately appeared at 750 nm ($\varepsilon = 8.23 \times 10^4$ L mol^{-1} cm^{-1}) and 760 nm (fluorescence quantum yield: 0.011), indicating that **FBC** could possess deep tissue penetrability. To confirm the deep penetration ability of **FBC**, tetrafluorophenyl chlorin (**FPC**) and tetraphenyl bacteriochlorin (**PBC**) with different absorption wavelengths were selected as the references (Fig. S8, ESI†). **FPC** and **PBC** were synthesized according to the previous literature[41,43] and the maximum absorbance wavelengths were 660 nm and 730 nm, respectively. The penetration ability was evaluated using 1,3-diphenylisobenzofuran (DPBF) as a probe by detecting the generation of ROS under light irradiation. DPBF can irreversibly react with ROS, leading to the decrease of the absorbance with the increase of illumination time (Fig. 1b). To mimic the penetration of light more accurately into tissues, pork skins with different thicknesses were utilized as barriers to evaluate the penetration ability of light with different wavelengths (Fig. 1c). As shown in Fig. 1d and S9–S11 (ESI†), it was observed that the degradation rate of DPBF with three solutions clearly decreased with pork skins. There is no significant difference between them with a 0.5 cm pork skin, since the absorbed light of three solutions all have good penetrating abilities to thin tissue. But the degradation rate of DPBF for **FBC** can still retain more than 60% with a 1.0 cm thick pork skin barrier, compared with the 27% retention for **FPC**. Thus, **FBC** has a remarkable penetration capability, which is beneficial to the treatment of deep tumors.

ROS production of FBC

The mechanism of ROS production of **FBC** under 750 nm light irradiation was further studied by using probes of ROS including singlet oxygen ($^1O_2$), superoxide ions ($O_2^{-\bullet}$) and hydroxyl radicals
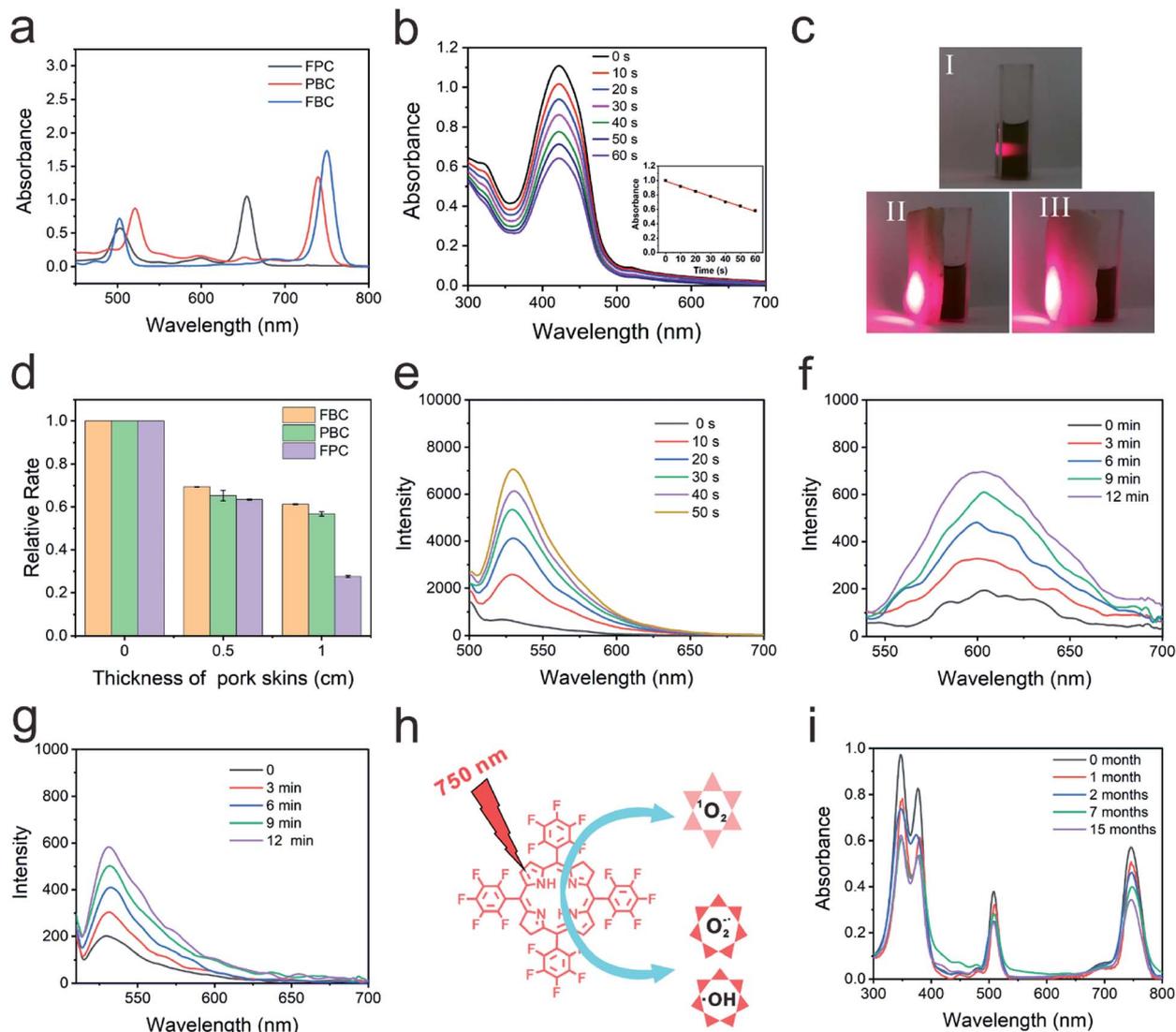
Fig. 1 Characterization of **FBC**. (a) UV-vis absorbance spectra of **FPC**, **PBC** and **FBC**. (b) UV-vis spectra of DPBF with increasing illumination time. The inset image shows the intensity changes at the maximum absorbance wavelength. (c) Photographs of **FBC** under laser irradiation with or without a barrier ((I) without a barrier; (II) with a 0.5 cm thick pork skin; (III) with a 1.0 cm thick pork skin). The degradation rates of DPBF in **FPC** (655 nm), **PBC** (730 nm) and **FBC** (750 nm) under laser irradiation (50 mW cm^{-2}) with or without different thicknesses of pork skins (d). Fluorescence spectra of (e) SOSG, (f) DHE and (g) HPF for $^1O_2$, $O_2^{-\cdot}$ and $\cdot OH$ detection with increasing illumination time (750 nm, 50 mW cm^{-2}), respectively. (h) Schematic of ROS production. (i) The UV-vis absorbance spectra of **FBC** at different times.

($\cdot OH$).[44–46] First, Singlet Oxygen Sensor Green (SOSG) was used as a $^1O_2$ probe to detect generated $^1O_2$ (Fig. 1e), and the fluorescence emission of SOSG incubated with **FBC** increased gradually with the increase of the illumination time, which confirmed that the $^1O_2$ could be produced by **FBC** under light irradiation. The singlet oxygen quantum yield is 0.496, using tetraphenyl porphyrin (TPP) as the standard (Fig. S12, ESI†).[47] Then, dihydroethidium (DHE) as an $O_2^{-\cdot}$ fluorescent probe was employed to determine the generation of $O_2^{-\cdot}$, where DHE can be dehydrogenated by $O_2^{-\cdot}$ and emit red fluorescence at 610 nm. As shown in Fig. 1f, the fluorescence intensity increased significantly with the extension of illumination time, suggesting that $O_2^{-\cdot}$ could be effectively produced by **FBC**. In addition, the $\cdot OH$ production potential of **FBC** was also demonstrated using fluorescence emission spectra using hydroxyphenyl fluorescein (HPF) as an indicator (Fig. 1g).

The gradual increase of the fluorescence intensity of HPF revealed that **FBC** could successfully induce the formation of highly toxic $\cdot OH$. These consequences demonstrated that **FBC** can not only generate $^1O_2$ through a type II reaction, but also produce $O_2^{-\cdot}$ and $\cdot OH$ through a type I reaction. However, **FPC** almost did not result in the generation of $O_2^{-\cdot}$ and **PBC** could only generate modest $O_2^{-\cdot}$ as depicted in Fig. S13 and S14 (ESI†), respectively. Therefore, **FBC** would achieve excellent PDT even in hypoxic tumors.

Stability evaluation of FBC

In addition, stability is also a crucial parameter for an excellent photosensitizer. To evaluate the stability, **FPC**, **PBC** and **FBC** solutions were irradiated at 660, 730, and 750 nm, respectively, and the stability of the samples was detected by UV-vis spectroscopy. As

shown in Fig. S15 (ESI†), there is no significant change for **FPC** and **FBC** solutions with increase of light irradiation, except for the obvious decrease of the absorption intensity of **PBC** solution, revealing that **FPC** and **FBC** have superior light stability. Much more visual results could be seen from their photographs taken before and after laser irradiation, as displayed in Fig. S16 (ESI†). More importantly, **FBC** in the mixed solution (V_{DMF}/V_{water}, 1/99) was further evaluated under visible light at room temperature for more than one year (Fig. 1i). The strong characteristic absorbance peak of **FBC** could be well retained even after 15 months, which further confirms the excellent stability of **FBC**. Therefore, hypoxia-tolerant **FBC** with remarkable penetration capability and excellent stability would present promising clinical application for NIR-mediated PDT of deep tumors.

Synthesis of the FBC nanogel

Encouraged by the hypoxia tolerance, excellent stability and penetration ability, **FBC** was further reacted with SH-PEG-SH to form cross-linked **FBC** nanogels for improving the hydrophilicity and biocompatibility. The reaction could be simply carried out by stirring at room temperature due to the high reactivity of fluorophenyl groups of **FBC** and strong nucleophilicity of sulfhydryl groups.[48,49] The particle size of **FBC** nanogels could be tuned with the concentrations of reactants, which was determined by dynamic light scattering (DLS), and it can be found that the size of **FBC** nanogels increased with increasing the concentration (Fig. S17, ESI†). Therefore, we prepared two kinds of **FBC** nanogels with different sizes by varying the concentrations of reactants. **FBC** nanogels were characterized by DLS and transmission electron microscopy (TEM), respectively. As shown in Fig. 2a, the hydrodynamic sizes of two kinds of **FBC** nanogels measured by DLS were about 80 nm and 200 nm, and they were termed **FBC-80** and **FBC-200**, respectively. The **FBC-80** and **FBC-200** observed by TEM all showed a spherical morphology with homogeneous sizes of 50 nm and 180 nm, respectively (Fig. 2b and S18, ESI†), which were smaller than those obtained by DLS, probably resulting from the shrinkage of the hydration of PEG chains in TEM measurements. ^{1}H-NMR and ^{19}F-NMR spectra were also utilized to determine the formation of **FBC** nanogels (Fig. S19–S22, ESI†). By comparing the integration area of the signal at 3.64 ppm (protons of SH-PEG-SH) to that of 8.1 ppm (protons of **FBC**) from the ^{1}H-NMR spectra of **FBC** nanogels, **FBC** nanogels were formed using a 2 : 1 molar ratio of SH-PEG-SH and **FBC**. Moreover, the ^{19}F-NMR spectrum also showed that the characteristic peak of *p*-F completely disappeared in that of **FBC** nanogels, indicating that the *p*-F atoms were all replaced by the sulfhydryl groups of SH-PEG-SH. The photophysical properties of **FBC** nanogels were determined by utilizing UV-vis and fluorescence spectra as depicted in Fig. 2c and d. Both **FBC** nanogels have similar UV-vis absorbance and fluorescence emission behaviors to the small molecular **FBC**, indicating that the formation of nanogels has no impact on the photophysical properties of **FBC**. Then, the ROS ($^1O_2$, $O_2^{-\cdot}$ and $\cdot$OH) generation of **FBC** nanogels was also assessed using the corresponding probes under 750 nm light irradiation (Fig. 2d, e and S23, ESI†). The result is similar
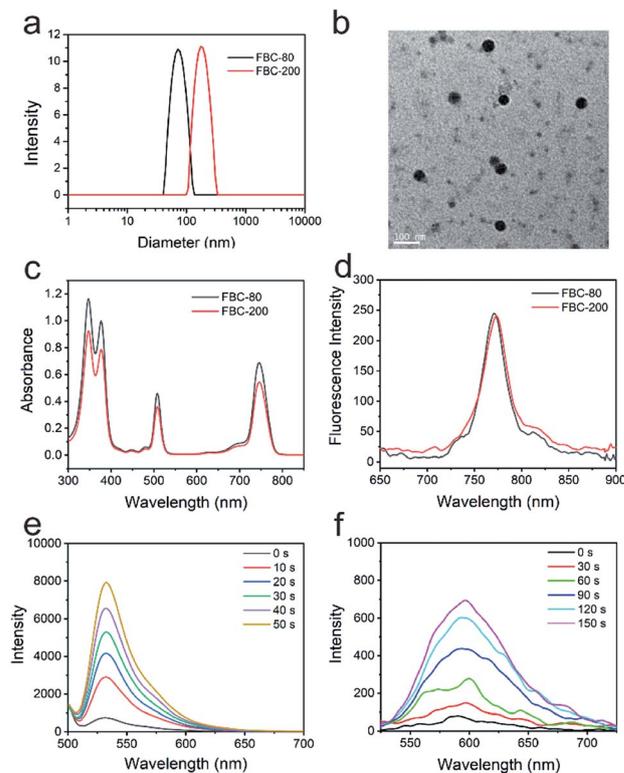

Fig. 2 Characterization of **FBC-80** and **FBC-200**. (a) Average hydrodynamic sizes of **FBC-80** and **FBC-200**. (b) TEM images of **FBC-80**. UV-Vis absorbance spectrum (c) and fluorescence emission spectrum (d) of **FBC-80** and **FBC-200**. Fluorescence spectrum of SOSG (e) and DHE (f) for $^1O_2$, $O_2^{-\cdot}$ detection with the increasing illumination time.

to that of **FBC**, suggesting that the formation of nanogels did not affect the ROS production capability of **FBC**. In addition, **FBC** nanogels could reduce the ACQ effect of PSs (Fig. S24 and S25, ESI†) and have excellent stability under physiological conditions (Fig. S26–S29, ESI†). Thus, the **FBC** nanogels should be suitable for NIR-mediated hypoxia-tolerant PDT.

Intracellular uptake and photoactivity

To evaluate the intracellular uptake of **FBC** nanogels, 4T1 cell lines were respectively co-incubated with **FBC**, **FBC-80** and **FBC-200** for 24 h. The cellular uptake of the samples was observed by confocal laser scanning microscopy (CLSM), where the nucleus was stained using Hoechst (blue fluorescence) and the samples were located through the red fluorescence produced by **FBC** itself. As shown in Fig. 3a, it can be observed that the red fluorescence appeared around the blue fluorescence, indicating that the samples were taken by the cells. Compared with those of **FBC**, the groups of **FBC** nanogels showed stronger fluorescence intensity, illustrating that more nanogels have been taken up by cells than the small molecular **FBC**.

To confirm the photodynamic performance of **FBC** nanogels against cancer cells, the intracellular ROS generation of **FBC** nanogels was evaluated as well (Fig. 3b). SOSG was used as a probe to detect the $^1O_2$, since it can be oxidized to produce green fluorescence by $^1O_2$. As demonstrated by CLSM in Fig. 3b, strong green fluorescence could be observed under laser
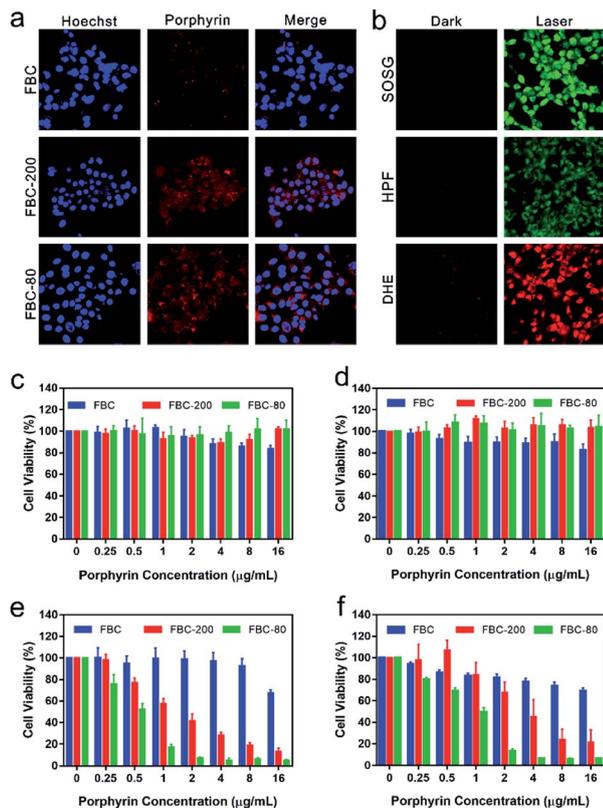
Fig. 3 *In vitro* PDT efficacy of **FBC-80** and **FBC-200**. (a) Confocal laser scanning microscope (CLSM) images of 4T1 cells treated with **FBC**, **FBC-200** and **FBC-80** for 24 h. (b) CLSM images of $^1O_2$, $^\cdot OH$ and $O_2^{-\cdot}$ in **FBC** nanogels-treated 4T1 cells using SOSG, HPF and DHE as detection probes, respectively. Cell viability of 4T1 cells treated with **FBC**, **FBC-200** and **FBC-80** without a laser in normoxic (c) and hypoxic (d) environments. Cell viability of 4T1 cells treated with **FBC**, **FBC-200** and **FBC-80** with a laser in normoxic (e) and hypoxic (f) environments.

irradiation, indicating that **FBC** nanogels can produce massive $^1O_2$ after 750 nm laser irradiation. In addition, HPF and DHE as specific ROS probes were separately employed to detect $^\cdot OH$ and $O_2^{-\cdot}$, which were generally produced through a less oxygen-dependent type I process of PDT. The bright fluorescence images of HPF and DHE are shown in Fig. 3b, meaning that a large amount of $^\cdot OH$ and $O_2^{-\cdot}$ was produced with light irradiation. Thus, **FBC** nanogels can be used as a potential nano-photosensitizer especially for a hypoxic environment.

Encouraged by the excellent cellular uptake and ROS production capability of **FBC** nanogels, the phototherapeutic effect of **FBC** was investigated by *in vitro* cytotoxicity assays. **FBC**, **FBC-200** and **FBC-80** with different concentrations were co-cultured with 4T1 cells, respectively. Cell viability was tested by a standard MTT assay in normal and hypoxic environments, respectively. As shown in Fig. 3c and d, the cells treated with the three samples all maintain a high cell survival rate under dark conditions. Moreover, **FBC** nanogels both showed higher cell viability compared with **FBC**, indicating that the introduction of hydrophilic PEG moieties endowed **FBC** nanogels with an excellent biocompatibility. The photodynamic efficiency was determined by using a 750 nm light source to irradiate cells for

15 min at a power density of 100 mW cm^{-2} (Fig. 3e and f). The viability of cells in all groups showed a concentration-related decrease whenever under normal and hypoxic conditions, indicating that **FBC** can produce ROS to cause cell death under illumination. Compared with those treated with **FBC**, cells treated with **FBC-200** and **FBC-80** showed a significantly lower survival rate, suggesting that **FBC** nanogels have a superior photodynamic therapeutic effect. This result may be attributed to the enhanced internalization of **FBC** nanogels. In addition, we found that **FBC-80** nanogels had the most efficient inhibition to cancer cells both under normal and hypoxic conditions, which could be resulting from the weak aggregation of **FBC** in **FBC-80** nanogels compared with **FBC-200** nanogels.

In vivo imaging and biodistribution, photodynamic therapy and bio-safety

In order to demonstrate the accumulation of **FBC** nanogels at the tumor site, a 4T1 tumor xenograft mouse model was chosen. Since **FBC** nanogels have a fluorescence emission in the near infrared region, the accumulation of **FBC** nanogels at the tumor site could be monitored in label-free methods by detecting the fluorescence of **FBC** itself. **FBC** nanogels were injected into tumor-bearing mice through the tail vein, and then the fluorescence images of nanogels were observed at 0.5 h, 4 h, 10 h, and 24 h post-injection. As shown in Fig. 4a, b and S30–S33 (ESI†), **FBC-80** and **FBC-200** both showed a strong fluorescence signal at the tumor site after 24 h, indicating that the nanogels could successfully accumulate into the tumor through the EPR effect. Subsequently, the *in vivo* anti-tumor therapeutic effect of **FBC** nanogels was studied. When the volume of the tumor xenograft in mice reached 100 mm^3, the mice were divided into five groups and injected with a 200 μL solution of different agents ($n = 4$ for each group): (1) PBS, (2) **FBC-80**, (3) **FBC-200**, (4) **FBC-80+L** and (5) **FBC-200+L** (porphyrin concentration at 1 mg kg^{-1}). At 24 h post injection, tumors of **FBC-80+L** and **FBC-200+L** groups were treated with 750 nm laser irradiation (200 mW cm^{-2}) for 10 min, respectively. In the period of treatment, the body weights of the mice and the volumes of the tumors were recorded every three days (Fig. 4c and d). There is no significant weight loss for all mice as shown in Fig. 4c, indicating that the **FBC** nanogels are biocompatible. The curves of relative tumor volume are shown in Fig. 4d. Compared with those in the control groups, the tumor growths in **FBC-80+L** and **FBC-200+L** groups were observed to be significantly suppressed after 15 days. In addition, the **FBC-80+L** group has better tumor suppression than the **FBC-200+L** group, indicating that **FBC** nanogels with a small particle size have a better photodynamic effect.[50] In order to further confirm the photodynamic therapeutic effect, the mice were sacrificed on the 15th day. The photograph of the tumors is displayed in Fig. 4e. The weights of the tumors are measured and recorded in Fig. 4f. From Fig. 4e and f, it can be seen that in the cases of treatment with **FBC** nanogels under light irradiation, the sizes and weights of the tumors changed significantly, which is consistent with Fig. 4d. These results confirm that **FBC** nanogels show excellent phototherapy against tumors. Among them, the **FBC-80+L** group
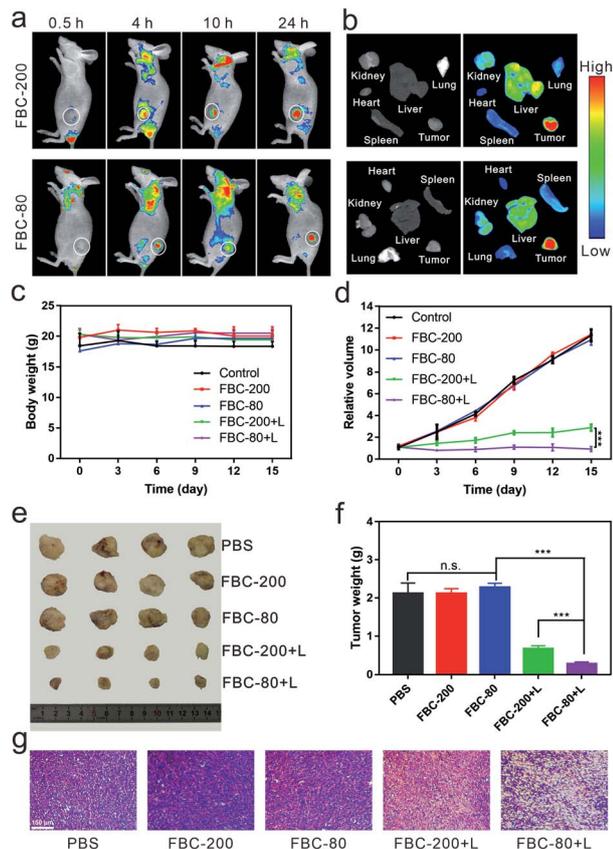
Fig. 4 *In vivo* PDT efficacy against 4T1 tumors. (a) Real-time fluorescence images of 4T1 tumor bearing mice after intravenous injection with **FBC-200** and **FBC-80**. (b) *Ex vivo* fluorescence images of major organs and tumors 24 h post i.v. injection. (c) Body weight. (d) Relative tumor volume. (e) Photographs of tumors. (f) Tumor weight. (g) H&E staining of tumors ($n = 4$, mean ± s.d., **$p < 0.01$, ***$p < 0.001$).

had the most significant tumor suppressive effect, indicating that the photodynamic therapy of **FBC** nanogels with a small particle size was the most effective among these groups.[51–53] Additionally, according to qualitative histological examinations (Fig. 4g), the most significant tumor necrosis was observed for the **FBC-80+L** group, which further confirmed the excellent photodynamic effect of **FBC-80** in inhibiting tumor growth. Besides, hematoxylin and eosin (H&E) staining of the major organ tissues is shown in Fig. S34 (ESI†). No obvious tissue damage was found in all organ tissues, revealing that the **FBC** nanogels are biocompatible.

Conclusions

In conclusion, we are inspired by the NIR absorption of natural bacteriochlorin to develop a novel bacteriochlorin-based photosensitizer **FBC**. In comparison to natural bacteriochlorin, **FBC** could be easily prepared by a two-step reaction from the original reactants pentafluorobenzaldehyde and pyrrole. Moreover, **FBC** exhibits an ultra-high stability even under visible light at room temperature for more than one year. **FBC** has strong NIR absorption at 750 nm, and its ROS generation capability can still retain around 60% with a 1.0 cm-thick pork skin as the barrier,

which is significant for the treatment of deep tumors. **FBC** could not only produce oxygen-dependent $^1O_2$, but also generate oxygen-independent ROS $O_2^-\cdot$ and OH$\cdot$, overcoming the bottleneck of PDT caused by tumor hypoxic microenvironments. Based on the promising properties of **FBC**, **FBC** nanogels were constructed by a simple crosslinking reaction with SH-PEG-SH. The formed **FBC** nanogels have a significant cumulative effect in the tumor site. Additionally, the **FBC** nanogels show a strong fluorescence emission in the NIR region, and thus distribution of drugs could be monitored using **FBC** itself. Finally, the excellent photodynamic efficacy of **FBC** nanogels has been revealed by *in vitro* and *in vivo* experiments. Therefore, **FBC** with superior properties would be a promising clinical photosensitizer for NIR-mediated hypoxia-tolerant PDT of deep tumors.

Ethical statement

All animal studies were conducted on male BALB/c nude mice (four to 5 weeks) in compliance with the National Institutes of Health Guide for the Care and Use of Laboratory Animals approved by the Animal Care and Use Committee of East China University of Science and Technology.

Conflicts of interest

There are no conflicts to declare.

Acknowledgements

References

1 Q. Wang, Y. Dai, J. Xu, J. Cai, X. Niu, L. Zhang, R. Chen, Q. Shen, W. Huang and Q. Fan, *Adv. Funct. Mater.*, 2019, **29**, 1901480.

2 K.-X. Teng, L.-Y. Niu, Y.-F. Kang and Q.-Z. Yang, *Chem. Sci.*, 2020, **11**, 9703–9711.

3 H. Deng, L. Lin, S. Wang, G. Yu, Z. Zhou, Y. Liu, G. Niu, J. Song and X. Chen, *Adv. Mater.*, 2019, **31**, 1903443.

4 K. Qiu, J. Wang, C. Song, L. Wang, H. Zhu, H. Huang, J. Huang, H. Wang, L. Ji and H. Chao, *ACS Appl. Mater. Interfaces*, 2017, **9**, 18482–18492.

5 Y. Shen, A. J. Shuhendler, D. Ye, J. J. Xu and H. Y. Chen, *Chem. Soc. Rev.*, 2016, **45**, 6725–6741.

6 S. Xu, X. Zhu, C. Zhang, W. Huang, Y. Zhou and D. Yan, *Nat. Commun.*, 2018, **9**, 2053.

7 M. Wang, Y. Zhang, M. Ng, A. Skripka, T. Cheng, X. Li, K. K. Bhakoo, A. Y. Chang, F. Rosei and F. Vetrone, *Chem. Sci.*, 2020, **11**, 6653–6661.

8 M. Lan, S. Zhao, W. Liu, C. S. Lee, W. Zhang and P. Wang, *Adv. Healthcare Mater.*, 2019, **8**, 1900132.

9 L. Lifshits, J. A. Roque III, P. Konda, S. Monro, H. D. Cole, D. von Dohlen, S. Kim, G. Deep, R. P. Thummel,

C. G. Cameron, S. Gujar and S. A. McFarland, *Chem. Sci.*, 2020, **11**, 11740–11762.

10 J. Li, D. Cui, Y. Jiang, J. Huang, P. Cheng and K. Pu, *Adv. Mater.*, 2019, **31**, 1905091.

11 Y. Chen, X. H. Zhang, D. B. Cheng, Y. Zhang, Y. Liu, L. Ji, R. Guo, H. Chen, X. K. Ren, Z. Chen, Z. Y. Qiao and H. Wang, *ACS Nano*, 2020, **14**, 3640–3650.

12 Y. Bu, T. Xu, X. Zhu, J. Zhang, L. Wang, Z. Yu, J. Yu, A. Wang, Y. Tian, H. Zhou and Y. Xie, *Chem. Sci.*, 2020, **11**, 10279–10286.

13 J. Zhao, L. Duan, A. Wang, J. Fei and J. Li, *WIREs Nanomed. Nanobiotechnol.*, 2020, **12**, 1583.

14 D. Cui, J. Huang, X. Zhen, J. Li, Y. Jiang and K. Pu, *Angew. Chem., Int. Ed.*, 2019, **58**, 5920–5924.

15 A. Sahu, K. Min, J. Jeon, H. S. Yang and G. Tae, *J. Controlled Release*, 2020, **326**, 442–454.

16 S. He, S. Lu, S. Liu, T. Li, J. Li, S. Sun, M. Liu, K. Liang, X. Fu, F. Chen, G. Meng, L. Zhang, J. Hai and B. Wang, *Chem. Sci.*, 2020, **11**, 8817–8827.

17 K. Ni, G. Lan, Y. Song, Z. Hao and W. Lin, *Chem. Sci.*, 2020, **11**, 7641–7653.

18 D. R. Hu, L. Zhong, M. Y. Wang, H. H. Li, Y. Qu, Q. Y. Liu, R. X. Han, L. P. Yuan, K. Shi, J. R. Peng and Z. Y. Qian, *Adv. Funct. Mater.*, 2019, **29**, 1806199.

19 W. Wang, Y. Cheng, P. Yu, H. Wang, Y. Zhang, H. Xu, Q. Ye, A. Yuan, Y. Hu and J. Wu, *Nat. Commun.*, 2019, **10**, 1580.

20 K. Zhang, Z. Yu, X. Meng, W. Zhao, Z. Shi, Z. Yang, H. Dong and X. Zhang, *Adv. Sci.*, 2019, **6**, 1900530.

21 Q. Wan, R. Y. Zhang, Z. Y. Zhuang, Y. X. Li, Y. H. Huang, Z. M. Wang, W. J. Zhang, J. Q. Hou and B. Z. Tang, *Adv. Funct. Mater.*, 2020, **30**, 2002057.

22 T. Luo, K. Ni, A. Culbert, G. Lan, Z. Li, X. Jiang, M. Kaufmann and W. Lin, *J. Am. Chem. Soc.*, 2020, **142**, 7334–7339.

23 Y. Wan, G. Lu, W. C. Wei, Y. H. Huang, S. Li, J. X. Chen, X. Cui, Y. F. Xiao, X. Li, Y. Liu, X. M. Meng, P. Wang, H. Y. Xie, J. Zhang, K. T. Wong and C. S. Lee, *ACS Nano*, 2020, **14**, 9917–9928.

24 P. A. Panchenko, M. A. Grin, O. A. Fedorova, M. A. Zakharko, D. A. Pritmov, A. F. Mironov, A. N. Arkhipova, Y. V. Fedorov, G. Jonusauskas, R. I. Yakubovskaya, N. B. Morozova, A. A. Ignatova and A. V. Feofanov, *Phys. Chem. Chem. Phys.*, 2017, **19**, 30195–30206.

25 Y. Y. Huang, P. Mroz, T. Zhiyentayev, S. K. Sharma, T. Balasubramanian, C. Ruzie, M. Krayer, D. Fan, K. E. Borbas, E. Yang, H. L. Kee, C. Kirmaier, J. R. Diers, D. F. Bocian, D. Holten, J. S. Lindsey and M. R. Hamblin, *J. Med. Chem.*, 2010, **53**, 4018–4027.

26 I. Roy, T. Y. Ohulchanskyy, H. E. Pudavar, E. J. Bergey, A. R. Oseroff, J. Morgan, T. J. Dougherty and P. N. Prasad, *J. Am. Chem. Soc.*, 2003, **125**, 7860–7865.

27 W. Liu, J. Zhang, Z. Zhou, D. Zhang, Y. Zhang, S. Xu and X. Zhu, *Adv. Mater.*, 2018, **30**, 1800403.

28 Y. Dong, Y. Tu, K. Wang, C. Xu, Y. Yuan and J. Wang, *Angew. Chem., Int. Ed.*, 2020, **59**, 7168–7172.

29 M. Yang, T. Yang and C. Mao, *Angew. Chem., Int. Ed.*, 2019, **58**, 14066–14080.

30 T. X. Zhang, Z. Z. Zhang, Y. X. Yue, X. Y. Hu, F. Huang, L. Shi, Y. Liu and D. S. Guo, *Adv. Mater.*, 2020, **32**, 1908435.

31 H. Zhang, H. Li, Z. Cao, J. Du, L. Yan and J. Wang, *J. Controlled Release*, 2020, **324**, 47–54.

32 K. Zhang, X. Meng, Z. Yang, H. Dong and X. Zhang, *Biomaterials*, 2020, **258**, 120278.

33 H. B. Cheng, Y. M. Zhang, Y. Liu and J. Y. Yoon, *Chem*, 2019, **5**, 553–574.

34 P. Gao, M. Wang, Y. Chen, W. Pan, P. Zhou, X. Wan, N. Li and B. Tang, *Chem. Sci.*, 2020, **11**, 6882–6888.

35 M. Li, X. Sun, N. Zhang, W. Wang, Y. Yang, H. Jia and W. Liu, *Adv. Sci.*, 2018, **5**, 1800155.

36 K. Sztandera, M. Gorzkiewicz and B. Klajnert-Maculewicz, *WIREs Nanomed. Nanobiotechnol.*, 2020, **12**, 1509.

37 L. H. Wu, X. J. Cai, H. F. Zhu, J. H. Li, D. X. Shi, D. F. Su, D. Yue and Z. W. Gu, *Adv. Funct. Mater.*, 2018, **28**, 1804324.

38 X. Zhang, X. Chen, Y. Guo, H. R. Jia, Y. W. Jiang and F. G. Wu, *Nanoscale Horiz.*, 2020, **5**, 481–487.

39 N. Liu, H. Liu, H. Chen, G. Wang, H. Teng and Y. Chang, *Colloids Surf., B*, 2020, **188**, 110753.

40 W. Zhu, Y. H. Gao, P. Y. Liao, D. Y. Chen, N. N. Sun, P. A. Nguyen Thi, Y. J. Yan, X. F. Wu and Z. L. Chen, *Eur. J. Med. Chem.*, 2018, **160**, 146–156.

41 Z. Liu, Y. Xue, M. Wu, G. Yang, M. Lan and W. Zhang, *Biomacromolecules*, 2019, **20**, 4563–4573.

42 Z. Liu, M. Wu, Y. Xue, C. Chen, F. R. Wurm, M. Lan and W. Zhang, *Chem. Commun.*, 2020, **56**, 2415–2418.

43 H. Cao, G. Wang, Y. Xue, G. Yang, J. Tian, F. Liu and W. Zhang, *ACS Macro Lett.*, 2019, **8**, 616–622.

44 A. Gollmer, J. Arnbjerg, F. H. Blaikie, B. W. Pedersen, T. Breitenbach, K. Daasbjerg, M. Glasius and P. R. Ogilby, *Photochem. Photobiol.*, 2011, **87**, 671–679.

45 H. M. Peshavariya, G. J. Dusting and S. Selemidis, *Free Radical Res.*, 2007, **41**, 699–712.

46 S. Tomizawa, H. Imai, S. Tsukada, T. Simizu, F. Honda, M. Nakamura, T. Nagano, Y. Urano, Y. Matsuoka, N. Fukasaku and N. Saito, *Neurosci. Res.*, 2005, **53**, 304–313.

47 R. W. Redmond and J. N. Gamlin, *Photochem. Photobiol.*, 1999, **70**, 391–475.

48 S. Gerlich, S. Eibenberger, M. Tomandl, S. Nimmrichter, K. Hornberger, P. J. Fagan, J. Tuxen, M. Mayor and M. Arndt, *Nat. Commun.*, 2011, **2**, 263.

49 R. A. Day, D. A. Estabrook, J. K. Logan and E. M. Sletten, *Chem. Commun.*, 2017, **53**, 13043–13046.

50 Y. Cai, D. Ni, W. Cheng, C. Ji, Y. Wang, K. Mullen, Z. Su, Y. Liu, C. Chen and M. Yin, *Angew. Chem., Int. Ed.*, 2020, **59**, 14014–14018.

51 W. Jiang, B. Y. Kim, J. T. Rutka and W. C. Chan, *Nat. Nanotechnol.*, 2008, **3**, 145–150.

52 H. Cabral, Y. Matsumoto, K. Mizuno, Q. Chen, M. Murakami, M. Kimura, Y. Terada, M. R. Kano, K. Miyazono, M. Uesaka, N. Nishiyama and K. Kataoka, *Nat. Nanotechnol.*, 2011, **6**, 815–823.

53 V. P. Chauhan, T. Stylianopoulos, J. D. Martin, Z. Popovic, O. Chen, W. S. Kamoun, M. G. Bawendi, D. Fukumura and R. K. Jain, *Nat. Nanotechnol.*, 2012, **7**, 383–388.